Materialia 21 (2022) 101327

Contents lists available at ScienceDirect

Materialia

journal homepage: www.elsevier.com/locate/mtla

Full Length Article

Real-time interface-tracking framework for the evolution of the phases during the quenching of the steel balls

Asghar Aryanfar[a,b,*], Jihad Jundi[a], S. Reza Damadi[c], William A. Goddard III[d]

[a] American University of Beirut, Riad El-Solh 1107 2020, Lebanon
[b] Bahçeşehir University, 4 Çırağan Cad, Beşiktaş, Istanbul 34353, Turkey
[c] University of Tabriz, 29 Bahman Blvd, Tabriz, Iran
[d] California Institute of Technology, 1200 E California Blvd Pasadena, CA 91125, United States

ARTICLE INFO

Keywords:
Quench
Phase transformation
Real-time evolution
Numerical modeling
Analytical development

ABSTRACT

The locus of the micro-structural phase boundaries and their respective volumetric fraction during the quench of the high-temperature austenite critically determines the resulted physical and mechanical properties. We have developed a new numerically dynamic framework and we have established analytical relationships, which combined with the experimental measurements, could predict the real-time formation of the *equivalent* phase borders and their marginal evolution within the steel ball throughout the quenching process. In this regard, the transient behavior of the temperature is computed upon quenching where the threshold of phase transformation, obtained from our experimental data, is tracked as the locus of the earliest formation of phase boundaries. Our parametric analysis predicts the role of the scale (i.e. radius) of the steel ball and the initial and quench (i.e. final) temperatures and additionally anticipates the onsets of parameters, where one and two of the phases cease to exist. The model could get utilized for the design of the quench parameters to obtain the desired mechanical properties from the original austenite state.

1. Introduction

Quench process is mainly used for hardening the steel by undergoing martensite transformation, where high-temperature austenite is rapidly cooled down through its eutectoid point, leading to destabilization [1,2]. This is a typical method resulting in the production of martensite steel [3] and the proper thermal treatment is needed to obtained the desired mechanical properties [4,5].

Ideally, the highest hardness value is attained from the formation of the highest possible content of martensite, where the pearlite and Bainite fraction are minimized. The produced steel is considered suitable for industrial applications [6–8], such as mining, where the forged steel balls are used to grind run of mine coarse materials in ball mills.

Since the cooling process always initiates from the boundary of the specimen, the surface will always be cooled down faster than the interior regions. Due to this constraint, the austenite will be transformed over multitude of temperatures, resulting in real-time variations in the amount of the formed microstructures and the overall mechanical properties of the specimen [9]. The successful quench leading to in the production of predominantly martensitic steel depends on the factors including the composition of the alloy (i.e. carbon fraction, etc), the quench medium (i.e. water at the specified temperature), and size and shape of the specimen [10]. Other phases could additionally get generated via continuous temperature variation [11,12].

In particular, the ultrafast treatment leads to micro-structural grain refinement and local chemical heterogeneities in the austenite ending in the formation of a large variety of micro-structural constituents upon quenching [13,14]. Meanwhile dual-phase (DP) steels which possess both soft and hard phases illustrate a combination of exchangeable strength and ductility with a high work-hardening rate [15] which is merely due to a better strain hardening behavior of the soft phase through the strong dislocation [16], the formation of twinning [17], and strain partitioning or strain-induced phase transformation [18,19].

Other factors additionally could alter the mechanical properties of the steel such as strain hardening [20], solute solution hardening/softening [21,22], precipitation strengthening [23]. The iron-carbon system the most important alloy utilized for engineering applications of steel [24], particularly when containing high density of dislocations with shorter average mean free path [25,26].

Nonetheless, the rate of quenching of austenite has a determining role on the amount of produced final microstructures and the overall mechanical properties [27] and the holistic approach for their real-time formation of has not been explored before.

* Corresponding author.
E-mail address: aryanfar@caltech.edu (A. Aryanfar).

https://doi.org/10.1016/j.mtla.2022.101327
Received 6 October 2021; Accepted 14 January 2022
Available online 16 January 2022
2589-1529/© 2022 Acta Materialia Inc. Published by Elsevier B.V. All rights reserved.

Table 1
Chemical composition of $70Cr2$.

C	Si	Mn	P	S	Cr	Mo	Ni	Al	Co	Cu	Fe
0.77	0.24	0.85	0.035	0.025	0.55	< 0.005	0.02	0.007	0.006	0.03	Base
Nb	Ti	V	W	Pb	Sn	B	Zr	Bi	As		
< 0.002	0.003	0.007	< 0.015	< 0.01	0.009	< 0.0008	0.004	< 0.01	0.01		

In this paper, a new framework is developed for the real-time evolution of the three distinct microstructures of Martensite, Bainite and Pearlite during the quench of the original austenite of the spherical geometry with the radius R from an initial temperature T_0 to the quench temperature T_q. Although the phases nucleate in spots randomly and grow in the rate determined by Avrami's [28,29] or Koistinen-Marburger [30] relationships, we simplify the model by considering the distinct phases separated by the equivalent phase borders[1] for the Bainite r_B and Pearlite r_P, developing in real-time. The role of the scale R, the quench T_q and initial T_0 temperatures, leading to the microstructural zone are quantified. Such analysis helps designing the required mechanical properties of the quenched austenite for achieving the specified ductility.

2. Methodology

2.1. Experimental

In order to obtain the temperature rate thresholds for the phase transformation, we have set up and performed quench experiments for several samples. The experimental balls are created from the $70Cr2$ type steel via the hot forging process. The spark atomic emission spectroscopy (ASTM E415) has been performed on the specimens via Foundry Master Smart Metal Analyzer Quantometer, Oxford Instruments Gbmh (Germany), as the standard test method for analysis of carbon and low-alloy steel. The resulted chemical composition is shown in the Table 1.

Before forging the samples were pre-heated in a furnace of temperature range $1000 - 1200°C$ and consequently through the mechanical pressing inside the warm steel molds to the diameter of $200mm$. After the molding the balls were exposed to the temperature of $950 - 1000°C$ and were cooled down continuously after. Next, the samples were quenched (without additional internal heating) via different water bath temperatures T_q, leading to variation in the type and fraction of the obtained microstructures. Afterwards, the samples were tempered in the $200 - 220°C$ for $1hr$ and finally were cooled down in the ambient temperature. Since the scale of the cooling tower (i.e. room size) is considerably large relative to the scale of the ball ($\approx 10cm$), therefore the temperature of the bath T_q does not vary tangibly during the cooling process. Moreover the cooling tower is temperature controlled with the water flow, which ensures the constant value of the quench temperature T_q.

In order to visually discern the microstructures, the samples were divided in the center via the wire cut instrument and were polished with the sand paper and alumina powder. The resulted surface was etched and prepared using Nital (98% Ethyl Alcohol, 2% Nitric acid) and was investigated subsequently via the optical microscope. The microstructures were formed approximately in 3 layers in the surface, middle and center locations. Figure 1a illustrates a cross section view of the cut piece of an experimental sample with the identified phase zones, where the identified phase concentration is the highest. A bare view from a sample is additionally included as the inset in this Figure. The respective closer-proximity micrographs from the outer, middle and central locations of a sample are illustrated in the Fig. 1b.

The time temperature transformation (TTT) diagram for initiation (nucleation of 0.1% of microstructures) is given in the Fig. 2 and the resulted continuous cooling transformation (CCT) diagram is illustrated in the Fig. 3 (both directly exported from JMatPro software). Additionally, the real-time thresholds of temperature rate $\left|\frac{\partial T}{\partial t}\right|$ for the transformation are obtained for both diagrams from the illustrated slopes in real-time, and qualitatively leads to the formation of the following phases from the outer region:

Martensite > Bainite > Pearlite

Table 2
Extracted phase transformation thresholds from the experimental figures.

	Trigger		Initial		Final	
Parameter	$\left\|\frac{\partial T}{\partial t}\right\|_B$	$\left\|\frac{\partial T}{\partial t}\right\|_P$	$\left\|\frac{\partial T}{\partial t}\right\|_B$	$\left\|\frac{\partial T}{\partial t}\right\|_P$	$\left\|\frac{\partial T}{\partial t}\right\|_B$	$\left\|\frac{\partial T}{\partial t}\right\|_P$
Exp. Threshold	50	23	0.275	1.2	0.005	0.003

The Jominy hardeneablity test was performed after the quench, and the phase fractions were extracted via the image processing tool Clemex [31]. The resulted steady state phase borders were approximated from the locus of the 50% Martensite/ 50% Bainite and 50% Bainite/ 50% Pearlite as the equivalent phase borders r_B and r_P respectively as shown in the Fig. 4. Additionally the hardness was measured in the radial distance toward the surface which is visualized in the Fig. 5.

2.2. Kinetic framework

We develop a $3D$ simulation framework for the formation of the microstructures from the original austenite in the spherical geometry, resembling the steel balls utilized in the mining industry.

The simulation has been performed in real-time, where the temperature distribution is determined via the heat transfer through the instantaneously-formed micro-structural layers. Accordingly, the equivalent phase borders r_B and r_P are obtained via the experimental thresholds obtained in the Table 2 and subsequently interpolated from the Fig. 3 for quantifying the equivalent zones of Martensite, Bainite and Pearlite, which in fact represents the highest concentration of the microstructural nuclei in the respective zone. Therefore such originally mixed-phase could get represented as a more ordered phase pattern illustrated in the Fig. 6a.

During the quenching of the original austenite, since the outer boundary of the specimen is affected by the cooling temperature and is the earliest to transform to the Martensite. This is followed by the formation of Bainite and Pearlite phases which form in the inner regions later on. The simulation of the phase transformation has been shown in the pseudo-chart shown in the Fig. 6b where a single-layer simulation has been performed for the original austenite followed by the 3-layer simulation upon the formation of the microstructure.

When a sample of initial temperature T_0 is thrown into the bath of quench temperature T_q, the transient behavior of the ball temperature T evolves both to the radial distance r and the time t, as the following:

$$\frac{\partial T_k}{\partial t} = \alpha_k(T)\left(\frac{\partial^2 T_k}{\partial r^2} + \frac{1}{r}\frac{\partial T_k}{\partial r}\right) \tag{1}$$

where $k \in \{A, M, B, P\}$ represents the three distinguished phases of Pearlite, Bainite and Martensite. The initial temperature is from the original austenite phase before quenching, hence:

$$T(r, 0) = T_0 \tag{2}$$

[1] A: Austenite, M: Martensite, B : Bainite, P : Pearlite.

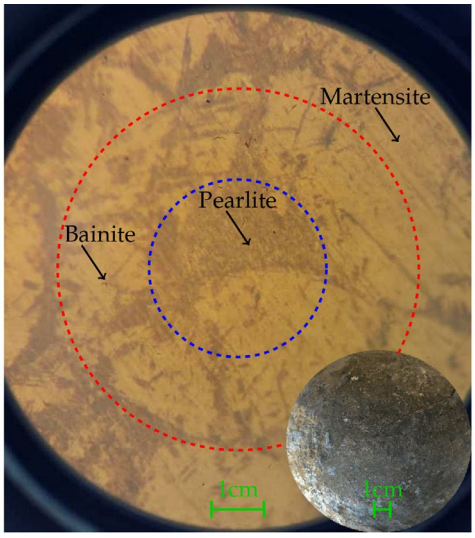

(a) Cross section of the the sample (inset: bare sample view)

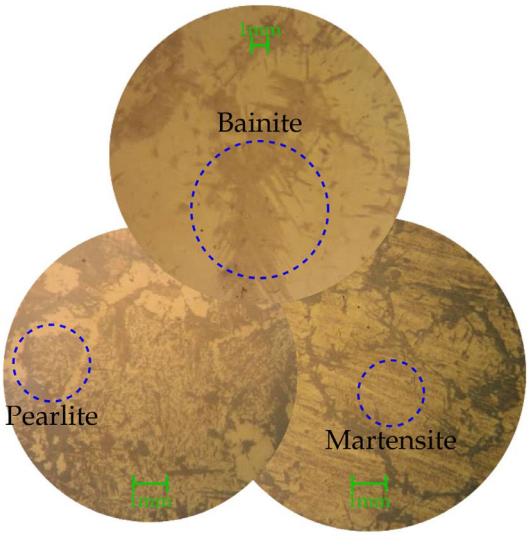

(b) Optical microscopy from the representative microstructures.

Fig. 1. Cross sectional image of an experimental sample (left) and the smaller scale images of the Martensite, Bainite and Pearlite (right).

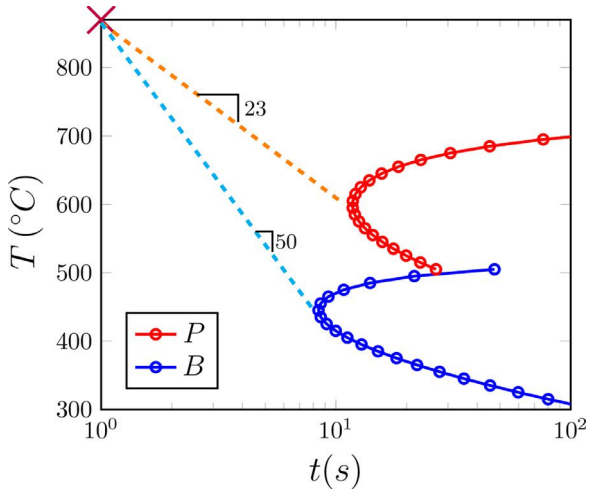

Fig. 2. Time temperature transformation (TTT) diagram for the triggering (nucleation of 0.1%) where the austenite starts transforming to the other microstructures.

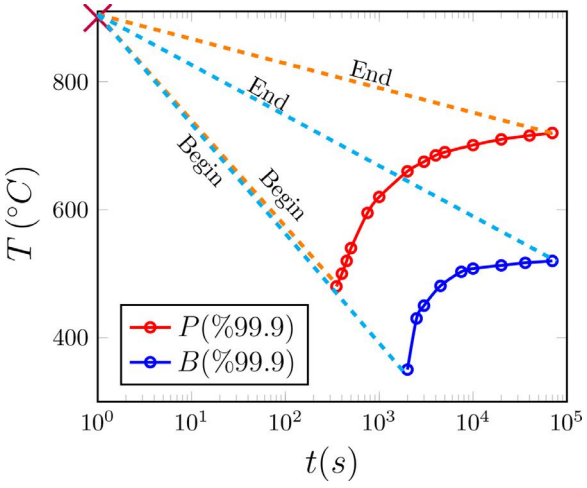

Fig. 3. Continuous cooling transformation (CCT) diagram for the phase transformation, utilized for the 3-layer simulation.

The outer boundary is connected to the water bath and remains at quench temperature T_q. Furthermore, since the temperature propagation occurs in the spherical medium, it should have have no variation in the center due to symmetry. Hence the boundary conditions are as:

$$\begin{cases} T(R,t) = T_q & \text{Quench temp.} \\ \dfrac{\partial T}{\partial r}(0,t) = 0 & \text{Symmetry} \end{cases} \tag{3}$$

Moreover, the temperature values should match in the interfaces of the neighboring microstructures, thus:

$$\begin{cases} T\left(r_P^-,0\right) = T\left(r_P^+,0\right) & \text{Pearlite continuity} \\ T\left(r_B^-,0\right) = T\left(r_B^+,0\right) & \text{Bainite continuity} \end{cases} \tag{4}$$

2.3. Numerical simulation

The pseudo-chart of the Fig. 6b has been explained in detail as below:

1. Assign the initial quench parameters as the initial temperature T_0. the quench temperature T_q and the scale of the austenite ball R.
2. Starting from the austenite of the specific heat diffusivity α_A, perform 1-layer simulation (Austenite Only) for the evolution of the temperature $T(r,t)$ and temperature rate $\frac{\partial T}{\partial t}$ profiles as a function of the radial distance r and time t, until the phase borders r_B and r_P forms.
3. Locate the equivalent phase borders r_B and r_P by tracking the temperature rate meeting the original thresholds of $\left|\frac{\partial T}{\partial t}\right|_P$ and $\left|\frac{\partial T}{\partial t}\right|_B$.
4. Initiating the values of r_B and r_P three distinct layers are formed respectively, which leads to updating the heat diffusivity values α_k based on the respective region for computing the temperature $T(r,t)$ in the subsequent steps.
5. Update the needed threshold for both Pearlite and Bainite $\left|\frac{\partial T}{\partial t}\right|_P$ and $\left|\frac{\partial T}{\partial t}\right|_B$.
6. Compute the temperature rate $\left|\frac{\partial T}{\partial t}\right|$ in the next time step and locate the updated values of r_B and r_P via comparing with the temperature

rate thresholds of Pearlite $\left|\frac{\partial T}{\partial t}\right|_P$ and Bainite $\left|\frac{\partial T}{\partial t}\right|_B$ in real-time from the Fig. 3.

7. Repeat steps 4 through 6 until the convergence of the equivalent phase borders r_B and r_P to a certain steady-state value.

The numerical simulations can be obtained using the finite difference method via moving forward in space (radial distance) r_i and time t^j $(FTFS)$. Therefore, for the Equation 1 and for the given phase k, one gets:

$$\frac{T_i^{j+1}-T_i^j}{\delta t}=\alpha_k\left(\frac{T_{i+1}^j+T_{i-1}^j-2T_i^j}{\delta r^2}+\frac{2}{r_i}\frac{T_{i+1}^j-T_i^j}{\delta r}\right) \tag{5}$$

re-arranging the above equation, one has:

$$T_i^{j+1}=Q_{1,i}T_{i-1}^j+Q_{2,i}T_i^j+Q_{3,i}T_{i+1}^j \tag{6}$$

where the Q_i's are the quotients defined as below:

$$\begin{cases}Q_{1,i}=\dfrac{\alpha_k\delta t}{\delta r^2}\\ Q_{2,i}=1-\dfrac{2\alpha_k\delta t}{\delta r}\left(\dfrac{1}{\delta r}+\dfrac{1}{r_i}\right)\\ Q_{3,i}=\dfrac{\alpha_k\delta t}{\delta r}\left(\dfrac{1}{\delta r}+\dfrac{2}{r_i}\right)\end{cases} \tag{7}$$

Performing tensor representation, the temperature in the time t_k could be explained as:

$$\mathbf{T}_{j+1}=\mathbf{Q}\mathbf{T}_j \tag{8}$$

where $\mathbf{T}$ and $\mathbf{Q}$ are temperature and coefficient tensors extracted respectively as below:

$$\mathbf{T}=\begin{bmatrix}T_1\\T_2\\\vdots\\T_{n-1}\\T_n\end{bmatrix}_{n\times1},\quad \mathbf{Q}=\begin{bmatrix}0&1&\dots&&0\\Q_{1,2}&Q_{2,2}&Q_{3,2}&&\vdots\\0&\ddots&\ddots&\ddots&0\\\vdots&&Q_{1,n-1}&Q_{2,n-1}&Q_{3,n-1}\\0&\dots&&0&1\end{bmatrix}_{n\times n},$$

$\mathbf{T}_0=\begin{bmatrix}T_0\\T_0\\\vdots\\T_0\\T_q\end{bmatrix}_{n\times1}$ and $\mathbf{T}_0$ is the initial condition tensor, where all the values are the initial temperature T_0 except the last value which is assigned continuously as the quench temperature T_q (i.e, boundary condition). Although the symmetry condition in the Eq. (3) is time-independent, the first row in the tensor $\mathbf{Q}$ is approximating that condition, particularly since the time segmentation δt is very small.

2.3.1. Numerical stability

In order to achieve the stable solution, the variation in the time δt should be small enough to capture the variation in the radial direction δr. For such criterion in the extreme case, one should have:

$$1-\frac{2\alpha_k\delta t}{\delta r^2}-\frac{2\alpha_k\delta t}{R\delta r}\geq0$$

re-arranging the above equation versus δr and solving the obtained quadratic inequality one gets:

$$\delta r\geq\sqrt{\left(\frac{\alpha_k\delta t}{2r_i}\right)^2+2\alpha_k\delta t}-\frac{\alpha_k\delta t}{2r_i} \tag{9}$$

Therefore it has to be valid for all the range of radius r_i, including the maximum value in the right hand side of the Eq. (9). The radius-dependent behavior can be obtained via taking the partial derivative of the left hand side with respect to radius r_m:

$$\frac{\partial(\delta r)}{\partial r_i}=\frac{\alpha\delta t}{\left(\left(\frac{\alpha_k\delta t}{2r_i}\right)^2+2\alpha_k\delta t\right)^{\frac{3}{2}}2r_i^4}+\frac{\alpha_k\delta t}{r_i^2}>0 \tag{10}$$

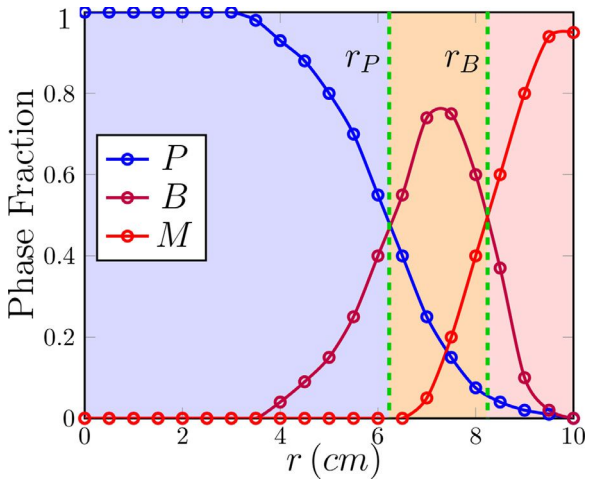

Fig. 4. A sample of phase fraction measurement along the radial direction.

which shows the monotonous increase in the space segmentation δr versus the radial distance r_i and therefore the largest limit could occur when $r_m\to\infty$:

$$\delta r_{\max}=\lim_{r_m\to\infty}\left(\sqrt{\left(\frac{\alpha_k\delta t}{2r_m}\right)^2+2\alpha_k\delta t}-\frac{\alpha_k\delta t}{2r_m}\right)=\sqrt{2\alpha_k\delta t} \tag{11}$$

Thus for the full solution stability one gets:

$$\delta t\leq\frac{\delta r^2}{2\alpha_k} \tag{12}$$

Performing the simulation and assigning the constants given in the Table 3, the temperature T profile is illustrated in the Fig. 7 and its respective transient development based on the couplings of the Eqs. (1)–(4) is shown in the Fig. 8. Regarding the temperature dependence of the heat conductivity α for the microstructures (Austenite, Martensite, Bainite and Pearlite), we have used their average values in the range of the original temperature T_0 and the quench temperature T_q from the respective temperature-dependent graphs [32].

Additionally, the temperature rate $\left|\frac{\partial T}{\partial t}\right|$ profile which determines the formation of microstructures and their respective boundaries is computed and illustrated in the Fig. 9. The evolution of these phase boundaries r_B and r_P from the thresholds given in the Table 2 is shown separately in the Fig. 10 where the dashed lines indicate the onset of final steady state values the simulation has converged to. The experimental data for the phase borders is supplemented in the same Figure.

The radius of the steel ball additionally has a critical role on the locus of the formed equivalent phase borders. This has been separately computed and is shown in the Fig. 11. Finally the variational effect of quench T_q and initial T_0 temperatures on the obtained steady-state phase boundaries is shown in the Fig. 12a and b.

2.4. Analytical solution

The temperature evolution $T(r,t)$, given in the Eq. (1) could additionally be approached analytically for comparison with the obtained computational trend. The form of the solution could be taken as a multiplication of sole temperature functions of radial distance $R(r)$ and the time $\Theta(t)$ by means of separation of variables as:

$$T(r,t)=R(r)\Theta(t) \tag{13}$$

For simplification one can assume that the evolution occurs in one layer (i.e. $\alpha_k:=\alpha$). Replacing the Eq. (13) into the Eq. (1) and dividing

Table 3
Simulation Parameters.

Parameter	Value	Unit	Ref.	Parameter	Value	Unit	Ref.
T_0	1173	K	Fig. 3	α_M	7.2	$mm^2.s^{-1}$	[32]
T_q	300	K	Fig. 3	α_B	6.6	$mm^2.s^{-1}$	[32]
R	10[a]	cm	Exp.	α_P	3.2	$mm^2.s^{-1}$	[33,34][b]
δr	0.25	mm	Assumed	α_A	5.4	$mm^2.s^{-1}$	[32]
δt	1.3	ms	Eq. (12)				

[a] Typical balls vary in diameter from 15mm to 120mm and are manufactured from scrap metal.
[b] https://www.aqua-calc.com/page/density-table/substance/pearlite

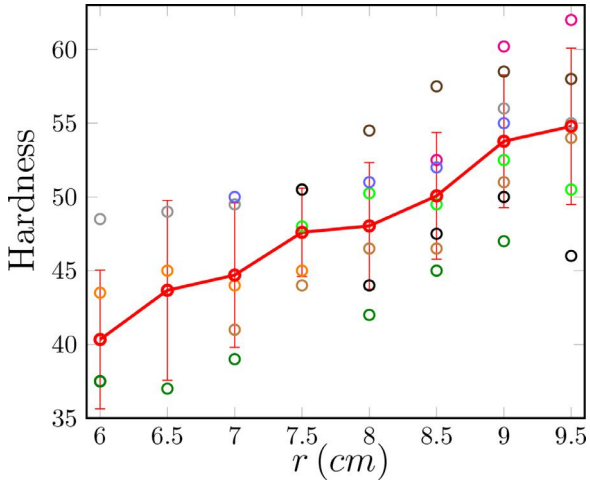

Fig. 5. The hardness measurements along the radial direction.

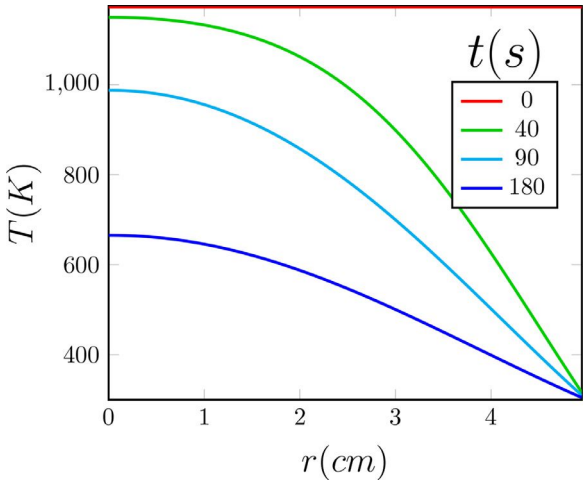

Fig. 7. Temperature profile $T(r,t)$ versus the radial distance r for different times t.

by the generic temperature form one gets:

$$\frac{\Theta'(t)}{\Theta(t)} = \alpha\frac{R''(r)}{R(r)} + \frac{2\alpha}{r}\frac{R'(r)}{R(r)} := -\lambda$$

The temperature decays from the initial temperature T_0 down to the final quench temperature T_q, throughout both radial distance and time. Since both $R(r)$ and $\Theta(t)$ are independent, the above relationship should be a constant of a negative value $-\lambda$. (i.e. $\lambda > 0$); hence the time-dependent equation for $\Theta(t)$ turns into:

$$\Theta'(t) + \lambda\Theta(t) = 0$$

From the Fig. 8 the solution has an exponential-decay form. Imposing the initial conditions of $\Theta(t \to 0) = T_0$ one gets:

$$\Theta(t) = T_0 \exp(-\lambda t) \tag{14}$$

respectively, the radial-dependent equation $R(r)$ turns into:

$$rR''(r) + 2R'(r) + \frac{\lambda}{\alpha}rR(r) = 0 \tag{15}$$

This is a unconventional differential equation form and the solution can be assumed in the form of indefinite series as:

$$R(r) = \sum_{n=0}^{\infty} a_n r^n \tag{16}$$

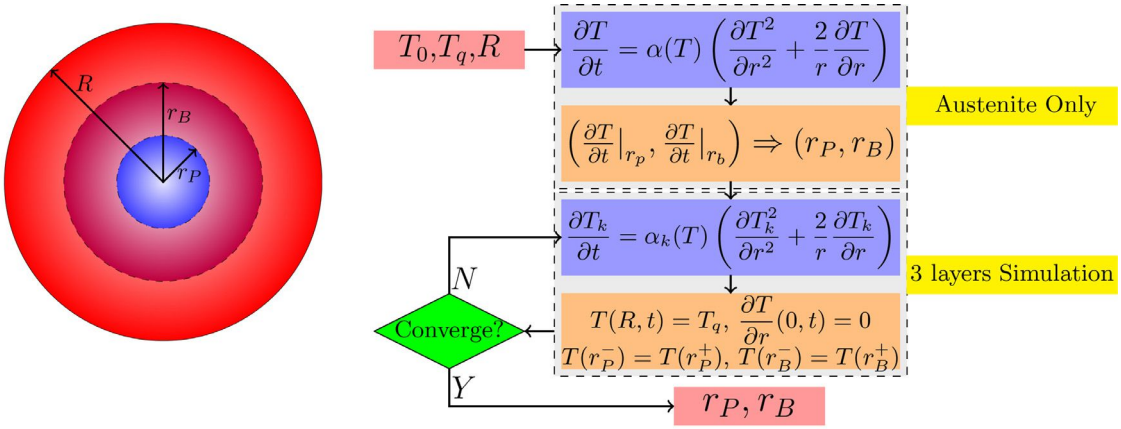

(a) Schematics of the equivalent phase borders r_B and r_P.

(b) Simulation Pseudo-chart.

Fig. 6. Characterizing the equivalent phase borders r_B and r_P with the radius R (left) and the respective simulation pseudo-chart (right).

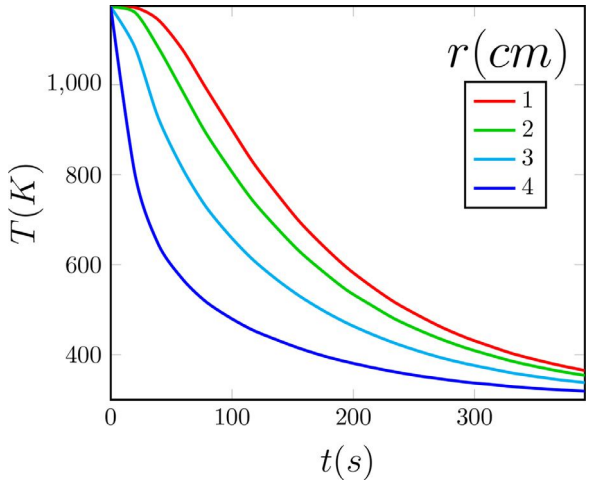

Fig. 8. Temperature decline $T(r,t)$ in time t for various radial positions r.

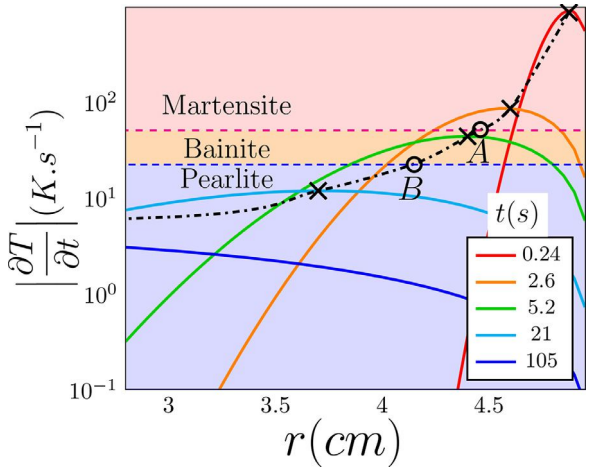

Fig. 9. Temperature rate $\left|\frac{\partial T}{\partial t}\right|$ profile versus radial distance r at various moments t for the triggering (0.1% of nucleation) of the microstructures. .

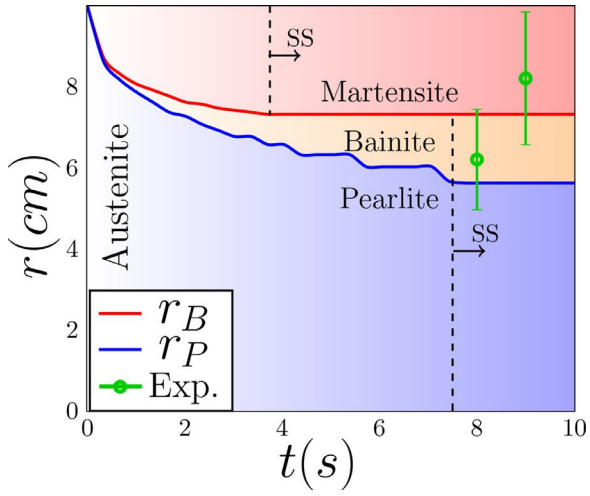

Fig. 10. The real-time formation of equivalent micro-structural borders r_B and r_P over time t until converging to the steady-state ss, which is compared with the steady-state experimental values, approximated from Fig. 4.

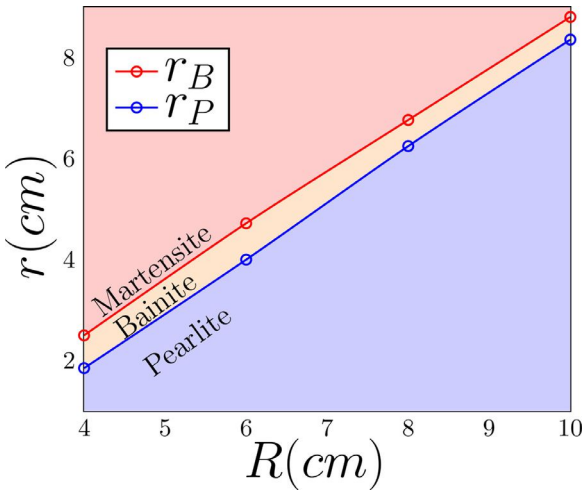

Fig. 11. The converged equivalent borders r_B and r_P to the steady-state ss versus the scale R.

Taking the first and second derivatives, one gets:

$R'(r) = \sum_{n=1}^{\infty} n a_n r^{n-1}$, $R''(r) = \sum_{n=2}^{\infty} n(n-1) a_n r^{n-2}$ replacing into the Eq. (15) and simplifying, one gets:

$$2a_1 + \sum_{n=1}^{\infty} \left((n+2)(n+1)a_{n+1} + \frac{\lambda}{\alpha} a_{n-1} \right) r^n = 0 \tag{17}$$

subsequently:

$$\begin{cases} a_1 = 0 \\ a_{n+1} = \dfrac{-\alpha}{\lambda (n+2)(n+1)} a_{n-1} \end{cases} \tag{18}$$

The first relationship is additionally obvious from the symmetric boundary condition in the Eq. (3) where $R'(0) = 0$; Therefore the odd-numbered coefficients turn zero ($a_{2n+1} = 0$) and regarding the even-numbered coefficients a_{2n} one gets :

$$a_{2n} = \frac{\alpha}{\lambda} \frac{(-1)^n \prod_{m=1}^{2n-1} (2m-1)}{(2n+1)!} a_0 \tag{19}$$

Assuming $a_0 = 1$ the final form is obtained as:

$$\begin{aligned} R(r) &= \sum_{n=0}^{\infty} \frac{\alpha}{\lambda} \frac{\prod_{m=1}^{2n-1} (2m-1)}{(2n+1)!} r^{2n} \\ &= \frac{\alpha}{\lambda} \left(1 - \frac{r^2}{2} + \cancel{O(r^4)} \right)^0 \end{aligned} \tag{20}$$

The reason for negligence of higher order power of radius is due to small value of r. Since $r \sim cm$ therefore $r < 1m$ and hence the higher powers become indefinitely closer to zero (i.e. $O(r^{2n}) \to 0$). Imposing the boundary condition in the outer boundary of the ball $R(R) = T_q$, one gets the power coefficient λ explicitly as a function of heat diffusivity α and the ball radius R as:

$$\lambda = \frac{\alpha}{T_q} \left(1 - \frac{R^2}{2} \right) \tag{21}$$

Finally the form of the solution and naming the new coefficient turns as:

$$T(r,t) \approx \beta \left(1 - \frac{r^2}{2} \right) \exp\left(-\frac{\alpha}{T_q} \left(1 - \frac{R^2}{2} \right) t \right) \tag{22}$$

where β is the constant obtained by merging the coefficients of $\Theta(t)$ and $R(r)$. Note that this approximation is valid for small r values $r < 1m$ where r^4 and higher terms could relatively get omitted.

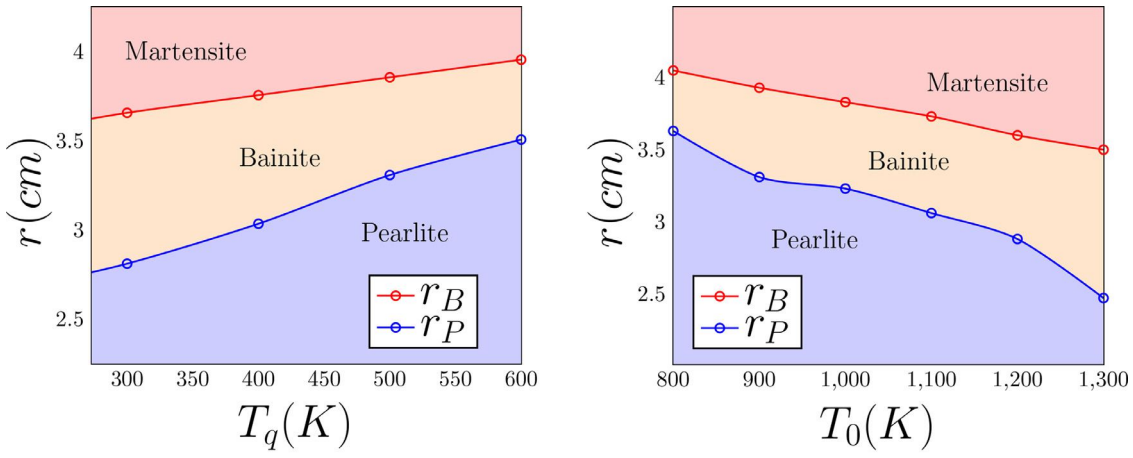

(a) Quench Temperature T_q. (b) Initial Temperature T_0.

Fig. 12. Variation in the steady-state equivalent borders of pearlite r_P and bainite r_B versus the initial T_0 and quench T_q temperatures.

3. Results & discussion

The analytical trend obtained in the Eq. (22) very well describes the temperature profiles in time and the transient behavior obtained versus radial distance in the Figs. 7 and 8. In fact the trend in the Fig. 7 has quadratic form as:

$$T(r) \sim 1 - \frac{r^2}{2} \tag{23}$$

where the negative coefficient of the highest power means the symmetric declining behavior, moving away from the center. ($r \uparrow \Rightarrow T \downarrow$) and the Fig. 7 describes a parabolic decrease, starting from the center as the peak position.

Time-wise the temperature trend in the Fig. 8 well-describes the exponential-decay behavior ($t \uparrow \Rightarrow T \downarrow\downarrow$), obtained analytically in the Eq. (14) as:

$$T(t) \sim \exp\left(-\frac{\alpha}{T_q}\left(1 - \frac{R^2}{2}\right)t\right) \tag{24}$$

Here the time-dependent decay rate for the temperature depends highly on the quench temperature T_q, the scale of the steel ball R and the heat diffusivity α of the quenched austenite.

As the amount of the formed-martensite M relies on the temperature decay-rate, one can discern the following relationships from the Eq. (24):

$$R \uparrow \Rightarrow \frac{\partial T}{\partial t} \downarrow \sim M \downarrow \text{ (more Ductile)}$$

$$\alpha \uparrow \Rightarrow \frac{\partial T}{\partial t} \uparrow \sim M \uparrow \text{ (more Brittle)}$$

$$T_q \uparrow \Rightarrow \frac{\partial T}{\partial t} \downarrow \sim M \downarrow \text{ (more Ductile)}$$

The first Equation here is obvious since for larger steel ball, more heat would be needed to reach the threshold of phase transformation, leading to the decrease in the martensite fraction. The second Equation is additionally obvious, since higher heat diffusivity means quicker temperature variation and the amount of martensite increases. The last equation means that the higher quench temperature T_q leads to a lower total temperature difference (i.e. $T_0 - T_q$). Therefore the temperature variation occurs slower, leading to less fraction of the martensite M.

Figure 9 indicates that the fastest rate of temperature $\left|\frac{\partial T}{\partial t}\right|$ across the spherical medium occurs in the initial moments of quenching in the outer regions of the ball. This is expected since the difference between the initial temperature T_0 and the quench temperature T_q is quite large and starts from the boundary. Throughout the time, such difference diminishes, resulting in the decrease of the temperature rate $\left|\frac{\partial T}{\partial t}\right|$. However, the cooling process will cause the temperature rate $\left|\frac{\partial T}{\partial t}\right|$ closer the central regions to increase and the peak value moves toward the center.

The outcome of the trend shown in the Fig. 9 would be the formation of a thin layer of martensite in the outer shell of the ball during the initial moments of the quench ($\sim 0 - 5s$). After the first intersection point A, the temperature rate still remains sufficiently higher than the pearlite threshold, allowing the Bainite microstructure to form ($\sim 0 - 15s$). After the intersection point B of the peak with the second threshold, the temperature rate $\left|\frac{\partial T}{\partial t}\right|$ is significantly smaller, leading only to the formation of the pearlite microstructure.

The interpretation from such transition is that the equivalent borders of Bainite r_B and Pearlite r_P form early during the first few seconds of quenching ($\approx 15s$). Throughout the time, as the temperature approaches to the quench value T_q, the temperature rate $\left|\frac{\partial T}{\partial t}\right|$ will also get smaller and flattens out across the ball. The formation of the Pearlite will continue the longest relative to the two other phases until forming a stable composition and equivalent phase border. Given the parameters in the Fig. 2, the steady state regime occurs at $\approx 4s$ for Martensite and $\approx 7.5s$ for the Bainite and Pearlite as shown in the Fig. 10. Needless to mention that in this figure, initial phase is still austenite (shown by color gradient) and the aforementioned phases appear throughout the time. The experimental phase borders r_B and r_P have been estimated from the locus of the 50% Martensite/ 50% Bainite and 50% Bainite/ 50% Pearlite as shown in the Fig. 4 respectively.

Figure 11 shows that the initial boundaries r_B, r_P move radially outward from the center versus the scale of the ball R. The underlying reason is that the larger ball possesses larger internal energy and it takes more time to cool it down, reducing the resulted temperature rate $\left|\frac{\partial T}{\partial t}\right|$. Thus, while the volume of each phase increases, their respective fraction remains almost the same as the scale-dependent rate is constant (i.e. $\frac{dr_P}{dR}, \frac{dr_B}{dR}$). Hence, the Bainite and Pearlite equivalent borders show to correlate linearly with the scale of the ball R and therefore their respective *radial fraction* is preserved.

In fact, the increasing trend in the Fig. 11 is due to the fact that the rate of heat transfer q into the ball is proportional to the surface area $q \sim R^2$, the total mass of the ball m would correlate with the volume as $m \propto V \sim R^3$. Therefore, the transferred heat to the ball could be calculated based on the specific heat c_p as [35] $\dot{Q} = mc_p\frac{\partial T}{\partial t}$, therefore combining

these 3 equations one gets:

$$\frac{\partial T}{\partial t} \sim \frac{1}{R}$$

which means that for large sizes the added mass m scales larger than the added heat rate $\dot{Q}$. Therefore the induced temperature rate will decrease. Consequently, the locus of the temperature rate thresholds (Table 2) will reduce down with the scale of ball R and hence form earlier in the outer boundaries.

The spherical shape also has a critical role on the rate of temperature change $\left|\frac{\partial T}{\partial t}\right|$. Getting closer to the center, the remaining volume significantly shrinks, and hence the cooling process would occur faster. Such dynamics indicates that for the smaller scales, the phase margins r_P and r_B could occur deeper in the ball leaving a thicker Bainite and Martensite phases.

The simulations based on the Table 3 show that, for the large-enough radius values of $R >\approx 100cm$ the rate of cooling will not be fast enough to form Martensite and for $R >\approx 150cm$ the sole formed phase is Pearlite. This is due to the fact that the required transferred heat would be too large to reach the temperatures rates needed for the formation of Martensite and Bainite phases. Such trend could easily get extrapolated from the scaling behavior shown in the Fig. 11, where the slope variations are obtained as:

$$\begin{cases} \frac{dr_B}{dR} \approx 1.05 \\ \frac{dr_P}{dR} \approx 1.08 \end{cases}$$

and being more than unity $\left(\frac{dr_{B,P}}{dR} > 1\right)$ means that the outer layers (M, B) will move further out with the scale, pass the physical boundary of the ball and vanish consequently, leaving the pearlite at the only dominant phase.

The quench temperature T_q additionally has a critical role on determining the locus of the formed boundaries. The higher quenching temperature T_q means closer proximity to the initial temperature T_0 which forms a lower temperature difference. This leads to the slower dynamics in the temperature rate $\left|\frac{\partial T}{\partial t}\right|$ and there is more time for the formation of ordered crystalline microstructures (i.e. Pearlite and to the lower magnitude Bainite). The such case due to Fourier's law the heat flow q decreases, leaving the comprising boundaries r_P and r_B closer to surface [36] as shown in the Fig. 12a. In fact, the temperature variation always occurs in the following range:

$$T_q \le T \le T_0$$

and since only the temperature rate $\left|\frac{\partial T}{\partial t}\right|$ determines the equivalent borders of the phase boundaries r_P and r_B, the increase in the quench temperature T_q is equivalent to the decrease in the initial temperature T_0 and opposite trend is expected. Such symmetric behavior is computed and successfully shown in the Fig. 12b.

Its worth to mention that while the temperature rate $\left|\frac{\partial T}{\partial t}\right|$ is both function of time t and temperature T, the quench is relatively a fast process and the our time-dependent approach covers the kinetics aspect and the thermodynamics-based growing of the phases based on the temperature T per se, occurs gradually in the slower pace.

4. Conclusion

In this paper, the complementary numerical and analytical frameworks are developed for quantifying the evolution of the equivalent phases boundaries of Pearlite/Bainite r_P and Bainite/Martensite r_B upon quenching of the steel ball. Extracting the phase formation thresholds $\left|\frac{\partial T}{\partial t}\right|_B$ and $\left|\frac{\partial T}{\partial t}\right|_P$ experimentally and performing parametric studies, we have attained that for the large-enough scales $R \gtrsim\approx \{100, 150\}cm$, one or two of the early-occurring phases cease to exist due to lack of fast-enough temperature rate. We have deduced almost linear correlation between the boundaries r_P and r_B versus the scale R and we have quantified the microstructure zones based on the quench and initial temperatures T_q and T_0. The tensor-based developed framework could get utilized for the design process of quench setup to obtain desired fractions of the phases and their respective boundaries from the original austenite phase. The results can be used in the design of the multi-microstructural layered steel balls with the required toughness, where hardness would increase with the martensitic fraction and ductility would depend on the Pearlite fraction.

Data Availability

The row data for producing the results in this manuscript are freely available upon request from the corresponding author at aryanfar@caltech.edu.

Declaration of Competing Interest

The authors declare that they have no known competing financial interests or personal relationships that could have appeared to influence the work reported in this paper.

Acknowledgement

The authors would like to thank the generous support from American University of Beirut, Award No. 103950 and the Masri Institute Award No. 103919 for the student Jihad Jundi. The helpful discussions with Dr. Saeed Keshavarz from University of Tabriz is additionally acknowledged.

Supplementary material

Supplementary material associated with this article can be found, in the online version, at 10.1016/j.mtla.2022.101327.

References

[1] D.S. Mackenzie, History of quenching, Int. Heat Treat. Surf.Eng 2 (2) (2008) 68–73.
[2] K. Prabhudev, Handbook of Heat Treatment of Steels, Tata McGraw-Hill Education, 1988.
[3] B. Liscic, H.M. Tensi, L.C. Canale, G.E. Totten, Quenching Theory and Technology, CRC Press, 2010.
[4] J. Zhao, Z. Jiang, Thermomechanical processing of advanced high strength steels, Prog. Mater. Sci. 94 (2018) 174–242.
[5] R. Colás, G.E. Totten, Encyclopedia of Iron, Steel, and Their Alloys (Online Version), CRC Press, 2016.
[6] P.J. Ennis, Ferritic and martensitic steels for power plants, in: Structural Alloys for Power Plants, Elsevier, 2014, pp. 188–220.
[7] G. Krauss, Deformation and fracture in martensitic carbon steels tempered at low temperatures, Metall. Mater. Trans. B 32 (2) (2001) 205–221.
[8] G.A. Roberts, R. Kennedy, G. Krauss, Tool Steels, ASM international, 1998.
[9] A. Alavudeen, N. Venkateshwaran, J.W. Jappes, A Textbook of Engineering Materials and Metallurgy, Firewall Media, 2006.
[10] W.D. Callister Jr, D.G. Rethwisch, Callister's Materials Science and Engineering, John Wiley and Sons, 2020.
[11] H.K.D.H. Bhadeshia, J. Christian, Bainite in steels, Metall. Trans. A 21 (3) (1990) 767–797.
[12] S. Van Bohemen, J. Sietsma, The kinetics of bainite and martensite formation in steels during cooling, Mater. Sci. Eng. A 527 (24–25) (2010) 6672–6676.
[13] F.C. Cerda, B. Schulz, D. Celentano, A. Monsalve, I. Sabirov, R. Petrov, Exploring the microstructure and tensile properties of cold-rolled low and medium carbon steels after ultrafast heating and quenching, Mater. Sci. Eng. A 745 (2019) 509–516.
[14] T. Lolla, G. Cola, B. Narayanan, B. Alexandrov, S. Babu, Development of rapid heating and cooling (flash processing) process to produce advanced high strength steel microstructures, Mater. Sci. Technol. 27 (5) (2011) 863–875.
[15] C.C. Tasan, M. Diehl, D. Yan, M. Bechtold, F. Roters, L. Schemmann, C. Zheng, N. Peranio, D. Ponge, M. Koyama, et al., An overview of dual-phase steels: advances in microstructure-oriented processing and micromechanically guided design, Annu. Rev. Mater. Res. 45 (2015) 391–431.
[16] J. Kadkhodapour, S. Schmauder, D. Raabe, S. Ziaei-Rad, U. Weber, M. Calcagnotto, Experimental and numerical study on geometrically necessary dislocations and non-homogeneous mechanical properties of the ferrite phase in dual phase steels, Acta Mater. 59 (11) (2011) 4387–4394.

[17] B. He, H. Luo, M. Huang, Experimental investigation on a novel medium Mn steel combining transformation-induced plasticity and twinning-induced plasticity effects, Int. J. Plast. 78 (2016) 173–186.
[18] B. Ennis, E. Jimenez-Melero, E. Atzema, M. Krugla, M. Azeem, D. Rowley, D. Daisenberger, D. Hanlon, P. Lee, Metastable austenite driven work-hardening behaviour in a trip-assisted dual phase steel, Int. J. Plast. 88 (2017) 126–139.
[19] M.-M. Wang, C.C. Tasan, D. Ponge, A.-C. Dippel, D. Raabe, Nanolaminate transformation-induced plasticity–twinning-induced plasticity steel with dynamic strain partitioning and enhanced damage resistance, Acta Mater. 85 (2015) 216–228.
[20] H. Mecking, U. Kocks, Kinetics of flow and strain-hardening, Acta Metall. 29 (11) (1981) 1865–1875.
[21] A. Sato, M. Meshii, Solid solution softening and solid solution hardening, Acta Metall. 21 (6) (1973) 753–768.
[22] R. Tunney, N. Ridley, Tempering of high-purity and commercially based steels containing 10 wt-% tungsten or 5 wt-% molybdenum, Metal Sci. 13 (10) (1979) 585–590.
[23] T. Gladman, Precipitation hardening in metals, Mater. Sci. Technol. 15 (1) (1999) 30–36.
[24] D. Quesnel, A. Sato, M. Meshii, Solution softening and hardening in the iron-carbon system, Mater. Sci. Eng. 18 (2) (1975) 199–208.
[25] G. Krauss, Martensite in steel: strength and structure, Mater. Sci. Eng. A 273 (1999) 40–57.
[26] E. Abbasi, Q. Luo, D. Owens, A comparison of microstructure and mechanical properties of low-alloy-medium-carbon steels after quench-hardening, Mater. Sci. Eng. A 725 (2018) 65–75.
[27] S. Serajzadeh, Modelling of temperature history and phase transformations during cooling of steel, J. Mater. Process. Technol. 146 (3) (2004) 311–317.
[28] M. Avrami, Kinetics of phase change. i general theory, J. Chem. Phys. 7 (12) (1939) 1103–1112.
[29] M. Avrami, Kinetics of phase change. ii transformation-time relations for random distribution of nuclei, J. Chem. Phys. 8 (2) (1940) 212–224.
[30] D.P. Koistinen, A general equation prescribing the extent of the austenite-martensite transformation in pure iron-carbon alloys and plain carbon steels, Acta Metall. 7 (1959) 59–60.
[31] H. Azizi-Alizamini, M. Militzer, W.J. Poole, A novel technique for developing bimodal grain size distributions in low carbon steels, Scr. Mater. 57 (12) (2007) 1065–1068.
[32] M. Lyassami, D. Shahriari, E. Ben Fredj, J.-B. Morin, M. Jahazi, Numerical simulation of water quenching of large size steel forgings: effects of macrosegregation and grain size on phase distribution, J. Manuf. Mater. Process. 2 (2) (2018) 34.
[33] J. Chen, S. Chen, On thermal conductivity of an in-situ metal matrix composite-cast iron, in: Metal, Ceramic and Polymeric Composites for Various Uses, 2011, p. 211.
[34] W. Hagel, G. Pound, R. Mehl, Calorimetric study of the austenite: pearlite transformation, Acta Metall. 4 (1) (1956) 37–46.
[35] S.A. Taylor, R.D. Jackson, Heat capacity and specific heat, Methods Soil Anal. Part 1 Phys.Mineral. Methods 5 (1986) 941–944.
[36] G. Casati, Energy transport and the fourier heat law in classical systems, Found. Phys. 16 (1) (1986) 51–61.